Research Article

Characterization of mechanical properties and fracture mode of PLA and copper/PLA composite part manufactured by fused deposition modeling

Xinzhou Zhang[1,2] · Lan Chen[1,2] · Tom Mulholland[2] · Tim A. Osswald[2]

Abstract

In this paper, fused deposition modeling is used to process pure polylactic acid (PLA) and copper fiber reinforced PLA composite (Cu/PLA) specimen. Comparative experiments are performed on printed specimens of different raster angles (0°, 90°, 45°, 0°/90° and ± 45°, respectively). Tensile testing, dynamic mechanical analysis (DMA), and fracture surface analysis are employed to characterize all the specimens. The DMA exhibits remarkable improvement on storage modulus and loss tangent of Cu/PLA composite specimen. Due to the lower tensile strength and higher elasticity of Cu fiber compared with PLA, the tensile strength of Cu/PLA composite specimen decreases with the addition of Cu fiber, while the elongation-at-break increases. Both PLA and Cu/PLA specimens printed at a raster angle of 0° show highest tensile strength and dynamic mechanical properties, while the 90° raster angle with the lowest value. Fracture morphologies indicate that the failure of a specimen of 0° raster angle is intra-layer fracture, while inter-layer fracture occur in the specimen of 90° raster angle.

Keywords Fused deposition modeling · Raster angle · Mechanical property · Fiber reinforced polymer

1 Introduction

Additive Manufacturing (AM) is an advanced process that uses computer-aided design to create a part by adding materials layer by layer [1–3]. The application of AM has expanded into various fields, with medical, automotive, aerospace and bioengineering being the fastest growing sectors in the AM industry [4–6]. The main reason is that AM has advantages that cannot be underestimated compared to traditional manufacturing techniques, such as the manufacture of complex structures, the reduction of material waste, and the customization of products [7–11]. Fused deposition modeling (FDM) is the preferred technique that widely used in 3D printing plastic parts in the modern manufacturing world [12]. In a typical FDM process (Fig. 1a), filamentous materials such as thermoplastic, wax or metal fuses are extruded from heated nozzles and deposited at a fixed rate according to a predetermined trajectory of each layer. When the first layer is completed, the workbench is lowered by a layer thickness to deposit a new layer until the deposition of the part is achieved [13–15]. The mechanical characteristics of FDM parts depend on several build parameters [13–15], such as raster angle, build orientation, layer thickness, raster width, and raster to raster air gap, as shown in Fig. 1b. To reduce the cost of 3D printing, Jones et al. [16] introduced RepRap (a portmanteau of self-replicating rapid prototyper) three-dimensional (3-D) printers, which is an open-source technology. RepRaps have been used in several fields and will be widely used in the future due to the advantage of low-cost and open-source [17–19].
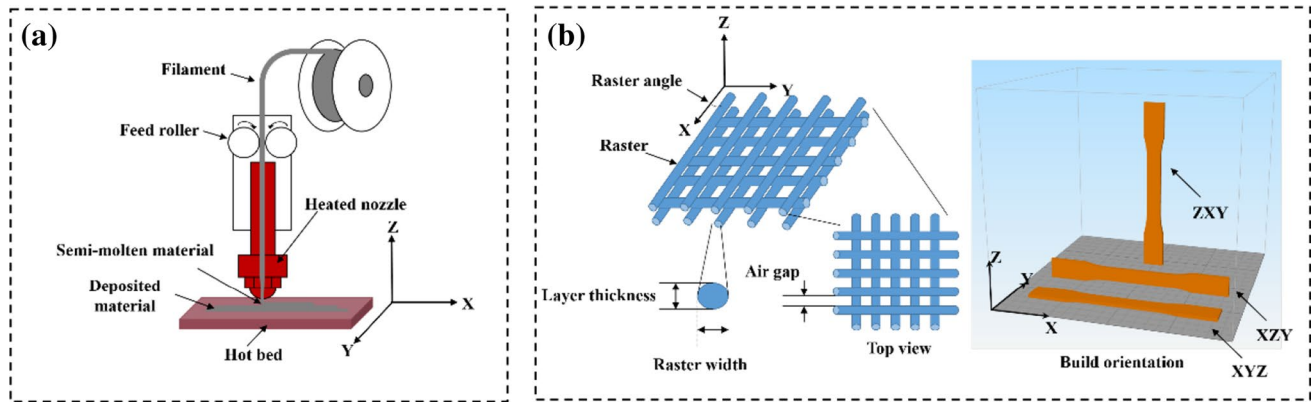
Fig. 1 **a** Schematic representation of a fused deposition modeling (FDM) system and **b** FDM build parameters

There are many materials that can be used for FDM printing. Currently, thermoplastic polymer materials (ABS, PC, PLA, PP) and thermosetting polymer materials (e.g. epoxy resins) are commonly used [20–24]. However, polymers are less suitable for industrial 3D printed parts due to the lack of required strength and functionality. To overcome these limitations, 3D printing of polymer composites has been introduced. Polymer composites exhibit enhanced structural and functional properties by the introduction of reinforcements, such as particles, fibers or nanomaterial [25–29]. The incorporation of reinforcing fibers into a polymer matrix for FDM printing creates a high performance functional composite part. Many researchers have performed studies in this area. Melenka et al. [30] evaluated the effect of different contents of fibers (4.04, 8.08, and 10.1 wt%, respectively) on the mechanical properties of FDM-printed nylon reinforced with continuous kevlar fibers. The results showed that the parts containing 10.1 wt% fiber had the highest stiffness and strength. Tekinalp et al. [31] studied the effect of fiber content on the mechanical properties of printed parts. They found that ABS/carbon fiber composites prepared by FDM showed an increased tensile strength and modulus as the fiber content increased, and a maximum increase of 115% and 700% could be obtained at 40 wt% carbon fiber. Shofner et al. [32] observed 39% increase in ultimate strength (from 26.9 to 37.4 MPa) and 86% reduction in strain at failure, when ABS was reinforced with 10 wt% vapor grown carbon fiber (VGCF). Zhong et al. [33] investigated the effect of short glass fibers on the mechanical properties of FDM printed parts. Their work demonstrated that ABS/glass fiber composite parts fabricated by FDM showed an increased tensile strength and decreased flexibility and handleability.

Although many researchers have studied the mechanical properties of thermoplastics with various fibers, there are few studies on composites with the metal fibers. The addition of metal fibers to the pure thermoplastic materials can improve various properties of the polymer. Some researchers have developed different metal reinforced plastic matrix composites and studied the thermal conductivity and radiation shielding properties of the polymer-metal composite parts [34, 35]. However, there is no comprehensive experimental study on the mechanical properties and dynamic behavior of FDM printed polymer-metal composite parts.

In this paper, pure polylactic acid (PLA) and copper fiber/polylactic acid (Cu/PLA) composites were selected as experimental materials for comparative experiments. Tensile tests and dynamic mechanical analysis (DMA) tests were performed on both PLA and Cu/PLA composite specimens. The influence of the FDM build parameters (raster angle) on the mechanical properties of all specimens was investigated. The fracture surface of the PLA and copper/PLA composite specimens at each raster angle was observed.

2 Experimental procedures
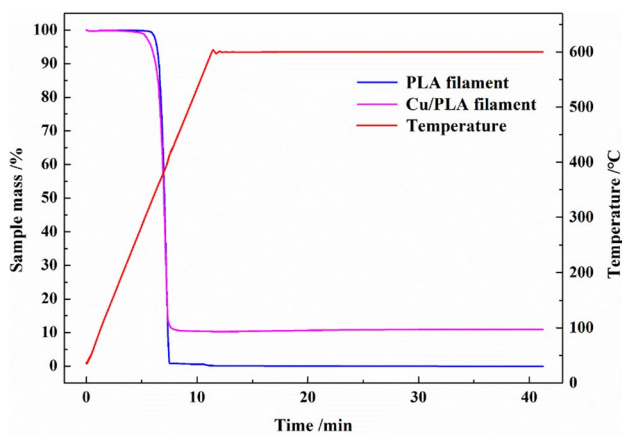
2.1 Materials

PLA and Cu/PLA filament were chosen to produce the specimen for test. The filament was provided by SainSmart (8021 Flint Street, Lenexa, Kansas, 66214, United States). The filament printing recommendations are listed in Table 1. The material property of Cu is shown in Table 2 as it is the key for the comparison between two materials. The Cu/PLA filament consisted of 10.35 wt% chopped copper fiber and PLA thermoplastic matrix. The real mass fraction of the material was measured with thermogravimetric analysis (TGA) in a Netzsch TG 209 F1 Libra (Fig. 2).

Table 1 The filament printing recommendations

Material	PLA	Cu/PLA
Diameter	1.75 mm (± 0.05 mm)	
Print temperature	200–240 °C	190–210 °C
Recommended platform temperature	40–60 °C	

Table 2 The properties of copper

Property	Cu
Nominal Size	10–20 μm
Density	8.96 g/cm^3
Melting point	1083 °C
Young's modulus	107.9 GPa
Hardness	35–45 HBS

Fig. 2 TGA curves of PLA and Cu/PLA filament under nitrogen atmosphere

Table 3 The FDM process parameters

Material	PLA	Cu/PLA
Nozzle diameter (mm)	0.4	
Nozzle extrusion temperature (°C)	220	200
Heat bed temperature (°C)	60	
Deposition layer height (mm)	0.2	
Deposition layer width (mm)	0.48	
Printing speed (mm/min)	1000	

2.2 Specimen fabrication

The FDM 3D printer (AON3D, 9494 Boul. St. Laurent Suite 600, Montreal QC, H2 N 1P4 Canada) was used to fabricate PLA and Cu/PLA composite specimens. The FDM building parameters in the paper are listed in Table 3. Specimens

for tensile and DMA test were prepared according to ASTM D638-14 and ASTM D5023-15 standard, respectively. The shape of the tensile specimen used was the type I tensile test bar (ASTM D638-14), having the length, width and thickness of 165, 19, and 3.2 mm, respectively. In this study, we mainly studied the influence of raster angle (0°, 90°, 45°, 0°/90° and ± 45°, respectively) on mechanical properties, as shown in Fig. 3. The size of DMA specimen was 50.8 mm × 12.7 mm × 1.6 mm. The raster angle was the same with the tensile specimen.

2.3 Material characterization

The dynamic mechanical properties of printed rectangular specimens (50.8 mm × 12.7 mm × 1.6 mm and raster angle of 0°, 0°/90°, ± 45°, 90° and 45°, respectively) were studied with a DMA instrument (EPLEXOR® DMA by NETZSCH GABO Instruments GmbH, Ahlden, Germany). The DMA was determined with a symmetric 3-point bending on a span of 30 mm as a function of temperature. Rectangular specimens were submitted to an oscillatory deformation (1 Hz) and a temperature gradient, from 30 to 175 °C, at a heating rate of a 1 °C/min. The storage modulus and loss modulus are calculated from the material response to the sine wave. At room temperature (∼ 20 °C), an Instron 5967 universal testing machine was used for tensile testing according to ASTM D638-14 standard. The load was applied at a rate of 5 mm/min. In order to obtain reliable tensile performance results, five specimens were used to test for each condition. Calculate the tensile stress by dividing the tensile load sustained by the specimen in newtons by the average original cross-sectional area in the gage length segment of the specimen in square meters. The strain is the change in grip separation relative to the original grip separation expressed as a percent. The fracture surface of the 3D printed specimens was performed by a LEO DSM 1530 field emission scanning electron microscope (FESEM). The cross-section of the filaments was also evaluated by SEM.

3 Results and discussion

3.1 Dynamic mechanical analysis

DMA is a technique that is widely used to characterize a material's properties. It is most useful for studying the viscoelastic behavior of polymers. Figures 4, 5 show dynamic storage modulus (E') and loss tangent (tan δ) as a function of temperature for PLA and Cu/PLA composite specimens.

The storage modulus of polymer denotes the elastic content of the material, which is affected by the polymer chain arrangement, the intermolecular force between
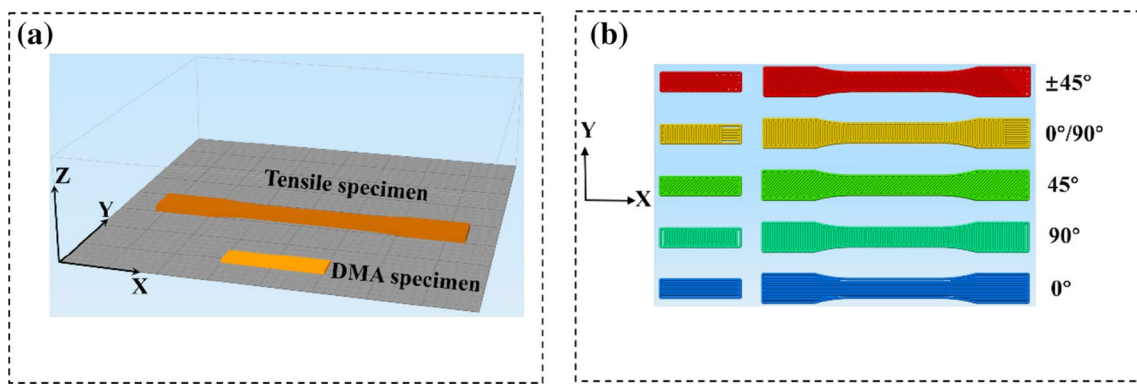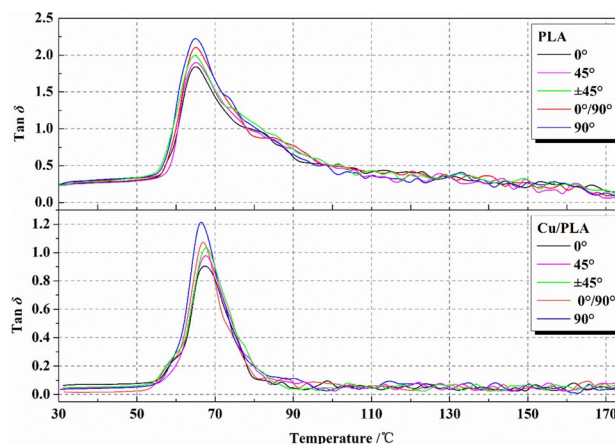
Fig. 3 Illustration of the **a** build orientations of specimens and **b** raster angles (0°, 90°, 45°, 0°/90° and ±45°)
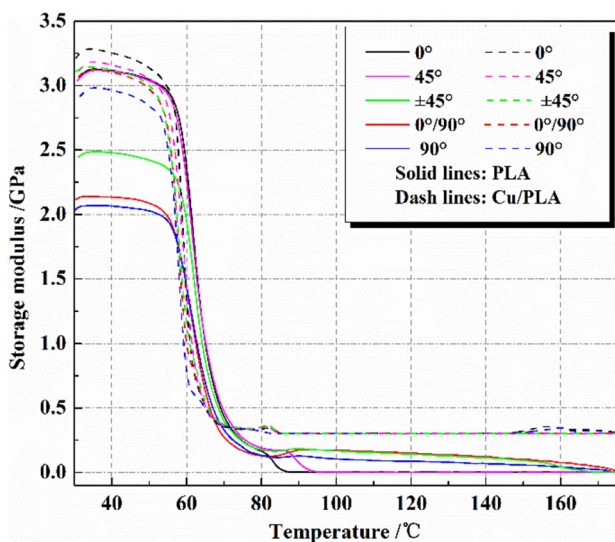
Fig. 4 Dynamic mechanical thermograms storage modulus of pure PLA and Cu/PLA composites as measured on 3D printed specimens (50.8 mm×12.7 mm×1.6 mm, raster angle of 0°, 0°/90°,±45°, 90° and 45°, respectively)

Fig. 5 Dynamic mechanical thermograms loss tangent of pure PLA and Cu/PLA composites as measured on 3D printed specimens (50.8 mm×12.7 mm×1.6 mm, raster angle of 0°, 0°/90°,±45°, 90° and 45°, respectively)

the fiber and the PLA matrix, and the stiffness of the fiber [36]. The storage modulus of PLA and Cu/PLA composite is shown in Fig. 4. For each specimen, three significant regions can be distinctively identified, namely glassy, transition and rubbery. At low temperature between 30 and 50 °C, the materials remain in a glass state. It is found that the Cu/PLA composite specimen of a certain raster angle has much higher storage modulus than the pure PLA of the corresponding raster angle during the glassy region. In Cu/PLA composites, the magnitude of the storage modulus is affected by the stiffness of the reinforcing fibers. The addition of Cu fibers to the PLA matrix increases the stiffness of the PLA and allows stress to transfer from the PLA matrix to the Cu fibers. Moreover, the raster angle has a significant effect on the storage modulus. The specimen printed at 0° raster angle has the highest value of

storage modulus followed by 45°,±45°, 0°/90° and 90° specimens, respectively. In transition region, all specimens show a gradual fall in value of storage modulus with the increase in temperature. When the temperature exceeds the glass transition temperature (Tg), the polymer chains begin to break. However, the softening temperature of Cu/PLA composite specimen is still higher than that of PLA. It might be due to the interaction of the Cu fiber and the PLA matrix resulting in a decrease of chain mobility.

The loss tangent is defined as the ratio of loss modulus to storage modulus, which represents the damping response of the material. The dependence of loss factor (tan δ) versus the temperature for pure PLA and Cu/PLA composite is shown in Fig. 5. Since the limitation of molecular motion is very poor at high temperature, pure PLA has the highest value of tan δ, indicating the best damping properties of the pure PLA. The lowest value of tan δ occurs in the Cu/PLA-0° specimen, followed by the

45°, ±45°, 0°/90° and 90°, specimens. Due to the strong interaction between the Cu fibers and the PLA matrix, the mobility of the macromolecules is reduced, and the stiffness of the material is improved, reflecting good load carrying capacity [37]. This indicates that the presence of Cu fibers in the polymer affects the damping response of the material. More importantly, the incorporation of Cu fibers moves the Tg peak to a higher temperature by 1.4 °C for 0° specimen (from 65.6 to 67 °C); 1.7 °C for 45° specimen (from 65.3 to 67 °C); 2.4 °C for ±45° specimen (from 64.9 to 67.3 °C), 2.1 °C for 0°/90° specimen (from 64.5 to 66.6 °C) and 1.2 °C for 90° specimen (from 64.4 to 65.6 °C). Shifting of Tg towards higher temperature of Cu/PLA composite shows the better thermal stability than pure PLA specimen [31].

3.2 Tensile properties

Figure 6 shows the stress–strain curves for the PLA and Cu/PLA specimens printed at 0°, 90°, 45°, 0°/90° and ±45°, respectively. The curve is selected from five specimens for each kind of FDM specimen. For pure PLA, it is observed that the stress increases almost linearly with the strain before breaking, indicating brittle nature of the material.

Interestingly, Cu/PLA stress–strain curves are different from the PLA. Initially, the stress–strain behavior is linear. After the stress reaches its peak, it is almost constant as the strain increases, indicating that the addition of Cu fiber into the PLA matrix changes fracture behavior from brittle to ductile fracture.

Effects of the raster angle on mechanical properties of all specimens are shown in Fig. 7. It can be observed that the raster angle results in different values of the tensile strength and Young's modulus for all PLA and Cu/PLA specimens. The 0° raster angle specimen is the one showing the best performance, while the 90° raster angle specimen is the one with the worst performance. The maximum tensile strength and Young's modulus recorded for PLA specimen with 0° raster angle are 68.1 MPa and 5.3 GPa, respectively, whereas for Cu/PLA specimen are 44.2 MPa and 5.1 GPa, respectively. Although Cu/PLA exhibits lower tensile strength and Young's modulus, the elongation-at-break appears a large improvement after the addition of Cu fiber (Fig. 7c). The improvement of elongation-at-break is 16.5%, 16.7%, 16.1%, 14.2% and 17.4% for FDM printed 0°, 45°, ±45°, 0°/90° and 90° specimens, respectively. Compared with pure PLA, the higher elasticity and lower tensile strength of Cu fiber can explain this phenomenon.
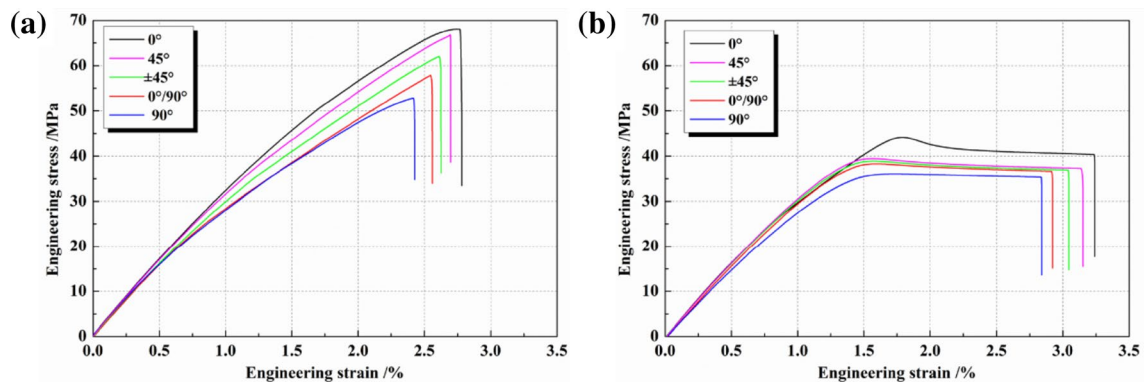

Fig. 6 Tensile stress–strain curves of **a** pure PLA and **b** Cu/PLA composite specimens
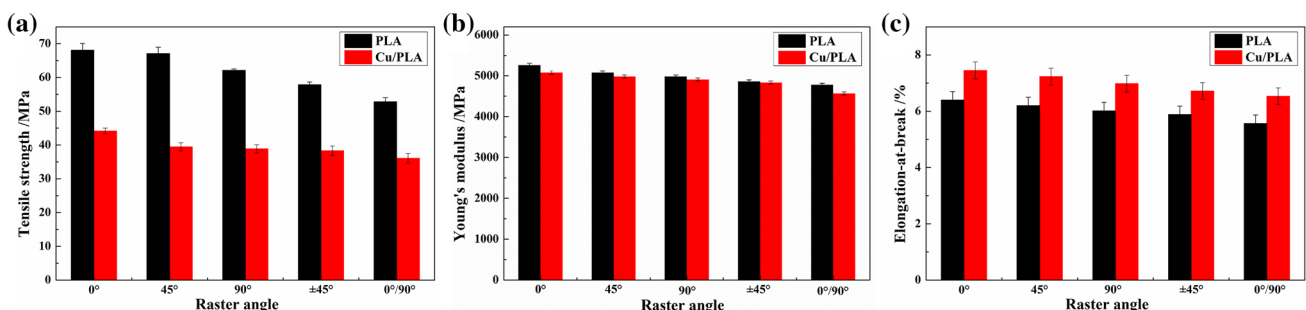

Fig. 7 Statistical histograms of the mechanical results of **a** tensile strength, **b** Young's modulus, and **c** elongation-at-break for pure PLA and Cu/PLA composite specimens

3.3 SEM observations

3.3.1 SEM observations of filament

Figure 8 shows cross-sectional SEM of PLA and Cu/PLA filaments, respectively. In order to obtain SEM specimens, the filaments are broken in liquid nitrogen. From Fig. 8a1 and a3, it is visible that the filament has a circular cross-section with a nominal diameter of 1.75 mm. Pure PLA (Fig. 8a2) exhibits a uniform smooth fracture surface. Seen from the fracture surface of the Cu/PLA, some Cu fibers embed in the PLA matrix and the surface is relatively rough (Fig. 8a4).

3.3.2 Fracture surface observations by SEM

According to the results of tensile test, the specimen printed at 0° raster angle has the best tensile properties. In order to explain this phenomenon, the fracture surfaces of all the specimens are observed by SEM.

Figure 9 shows the fracture surface SEM images of PLA and Cu/PLA at 0° raster angle with different magnifications.

Fig. 8 The cross-sectional SEM images of **a1**, **a2** PLA filament and **a3**, **a4** Cu/PLA filament
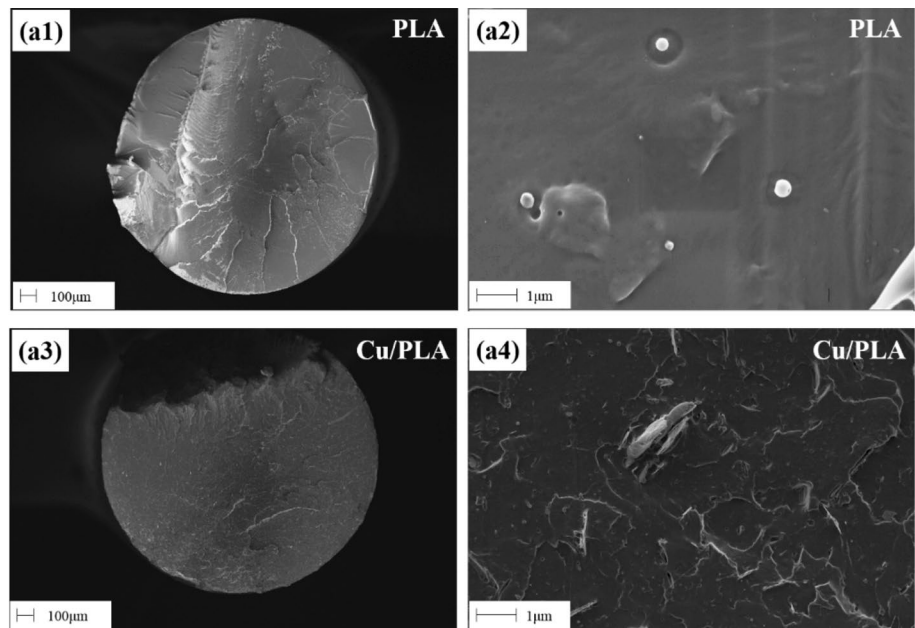
Fig. 9 Typical SEM images of fracture surface from failed FDM specimen at 0° raster angle. **a1**, **a2** PLA and **a3**, **a4** Cu/PLA
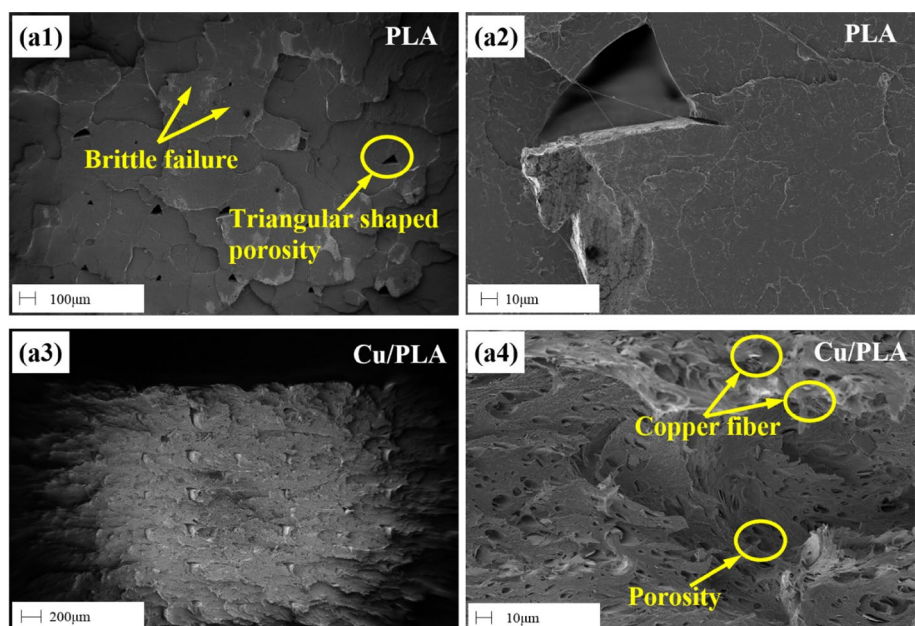
Figure 9a1 and a3 show the periodic structure of FDM processing. Some triangular shaped porosities appear between the raster layers, due to presence of stacking effects during FDM processing, resulting in material unfilled between the various fused deposition layers [38]. Due to the brittleness of pure PLA, no occasional necking are visible and the fracture surface exhibits relatively smooth properties. As shown in Fig. 9a3, the fracture surface Cu/PLA becomes rough with the addition of copper fibers. From the higher magnified images (Fig. 9a4), it can be seen that many white sheet-like copper fibers are distributed in the PLA matrix. In addition, some porosities with the same shape as the Cu fibers can be seen clearly. The Cu fibers are pulled out to leave these porosities in the fracture surface, indicating insufficient interfacial adhesion between the PLA matrix and the Cu fibers. When the tensile load is higher than the bond strength at the interface between the PLA and Cu fiber, the Cu fibers will be pulled out to form porosities. This is why the tensile strength of Cu/PLA is lower than that of PLA. In Fig. 9a4, some small porosities can be observed. It is obvious that these porosities are not caused by fiber pull-outs. Such porosities have also been reported in other literature and are referred to as gas porosity [39, 40]. The formation of the gas porosity may be due to the shrinkage of the specimen from the molten to the solid state during the FDM printing process. For 0° raster angle specimen, the individual raster fiber are aligned with tensile loading direction. The main stress is generated in each layer (intra-layer bonding) and until raster fibers of all layers is broken, the specimen will fail.

SEM images of PLA and Cu/PLA at 90° raster angle with different magnifications are shown in Fig. 10. In Fig. 10a1,

it can be clearly observed that the lateral direction of the raster layer deposited by FDM. The fracture occurs in the direction of the fuse line, namely the printing direction, and the fracture surface of the pure PLA is relatively smooth. In Fig. 10a2, with higher SEM magnification, fewer porosities and some protruding PLA filament appear on SEM images of fractured PLA specimens, indicating well adhesively bonded filament. The fractured surfaces of Cu/PLA composites have shown large copper fibers embed in the fracture surface.
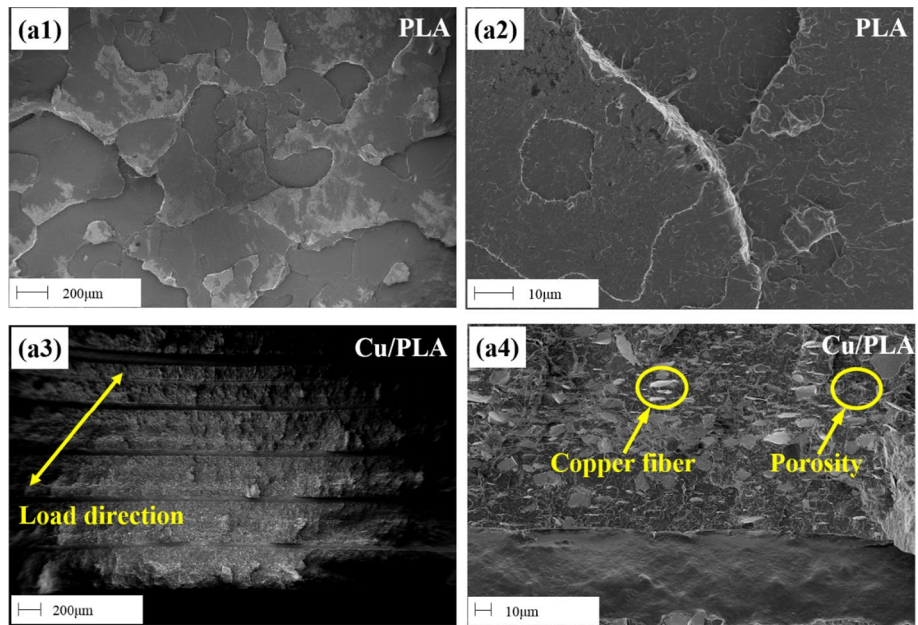
The fracture surface of FDM specimen fabricated at 45° raster angle is shown in Fig. 11. In order to get better SEM images, the fracture surface is rotated to a horizontal plane at an angle of 45° to the direction of the tensile loading. It can be found that the images may have some resemblance with the image at 90° raster angle. A similar phenomenon is observed on the fracture surface of PLA and Cu/PLA specimen at 45°, as shown in Fig. 11. Obviously, 45° raster layers are separated by delamination between successive layers. Free porosities are left on the fracture surface of PLA, as occurs with the Cu/PLA.

SEM images of tensile fractured surfaces of PLA and Cu/PLA at $\pm 45°$ are shown in Fig. 12. The fracture surface is perpendicular to the tensile load direction, which is different from the specimens printed at 45°. It can be seen that a large of micro-hills align 45° and delamination zone occur on the fracture surface of $\pm 45°$ specimen, indicating that $\pm 45°$ raster angle specimen fails under both inter-layer and intra-layer fracture. In Fig. 12, at high magnification, it can be easily noted that the reinforced copper fibers, as well as the porosities left by fiber pull-outs and other porosities.

Fig. 10 Typical SEM images of fracture surface from failed FDM specimen at 90° raster angle. **a1**, **a2** PLA and (**a3**, **a4**) Cu/PLA
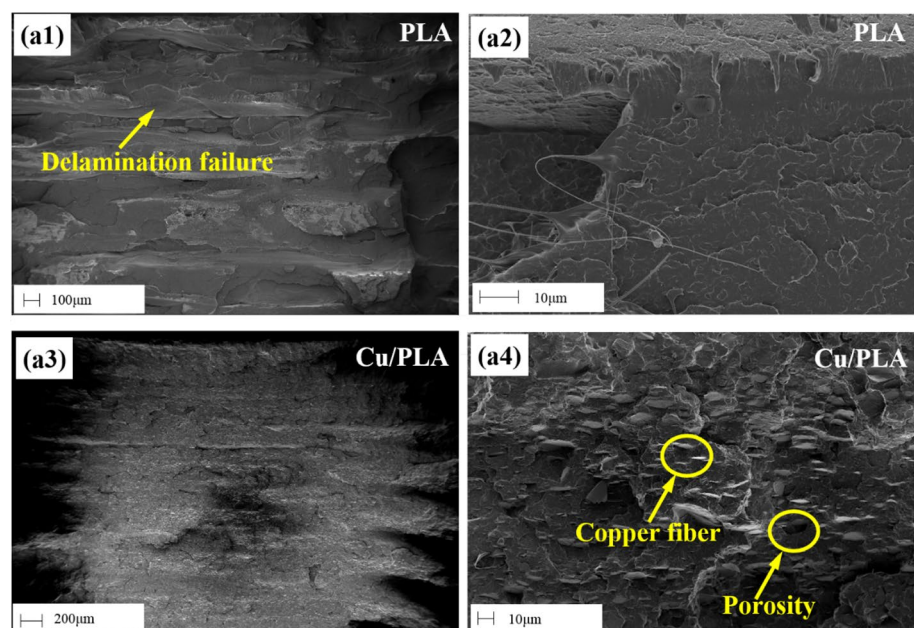
Fig. 11 Typical SEM images of fracture surface from failed FDM specimen at 45° raster angle. **a1**, **a2** PLA and **a3**, **a4** Cu/PLA

Fig. 12 Typical SEM images of fracture surface from failed FDM specimen at ± 45° raster angle. **a1**, **a2** PLA and **a3**, **a4** Cu/PLA
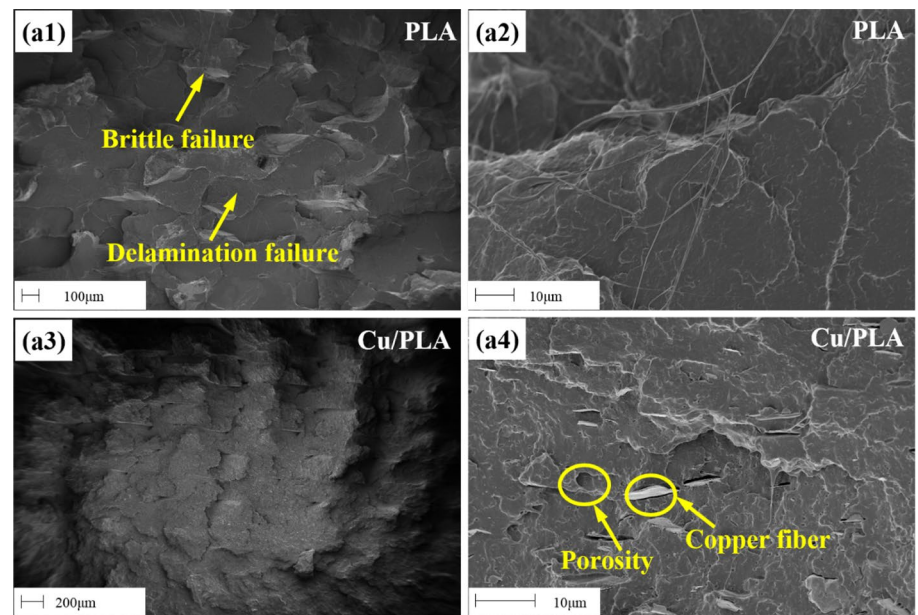

Figure 13 shows the morphologies on the fracture surface of failed PLA and Cu/PLA specimen at 0°/90°. The fracture morphology in Fig. 13 shows alternating distribution of 0° and 90° raster layers of the 0°/90° raster angle specimen, indicating different fracture behavior for 0° and 90° raster angle layers. Figure 13a1 reveals that numerous micro-hills appear on the 0° raster layers, indicating that the 0° raster layers fails by pulling off raster fibers. Whereas, the fracture surface of the 90° raster layers is relatively smooth, indicating that 90° raster layers detach from the adjacent raster layers. In addition, the failure first starts from 90° raster layers, and finally breaks at the 0° raster

layer. In Fig. 13a4, many cooper fiber particles and porosities also can be seen on the fracture surface of the Cu/PLA.

3.4 Study of fracture mechanism

The typical fracture modes of the specimens printed with different raster angles (at 0°, 90°, 45°, 0°/90° and ± 45°) are summarized in Fig. 14.

For 0° raster angle specimen, the individual raster layers are aligned with tensile loading direction (Fig. 14a). When tensile loading is applied, the main stress is generated in each layer. Each raster layer is composed of a

Fig. 13 Typical SEM images of fracture surface from failed FDM specimen at 0°/90° raster angle. **a1**, **a2** PLA and **a3**, **a4** Cu/PLA
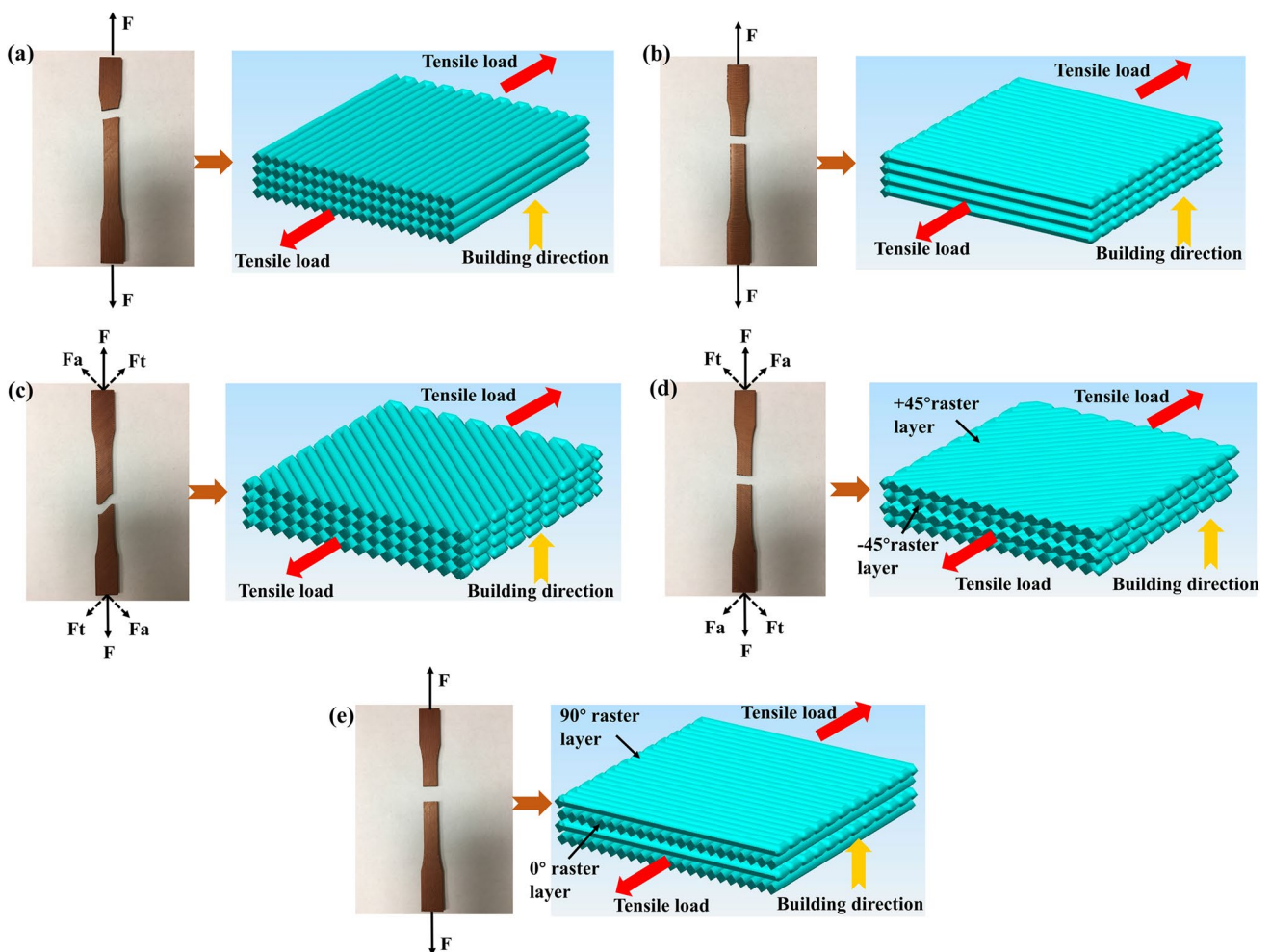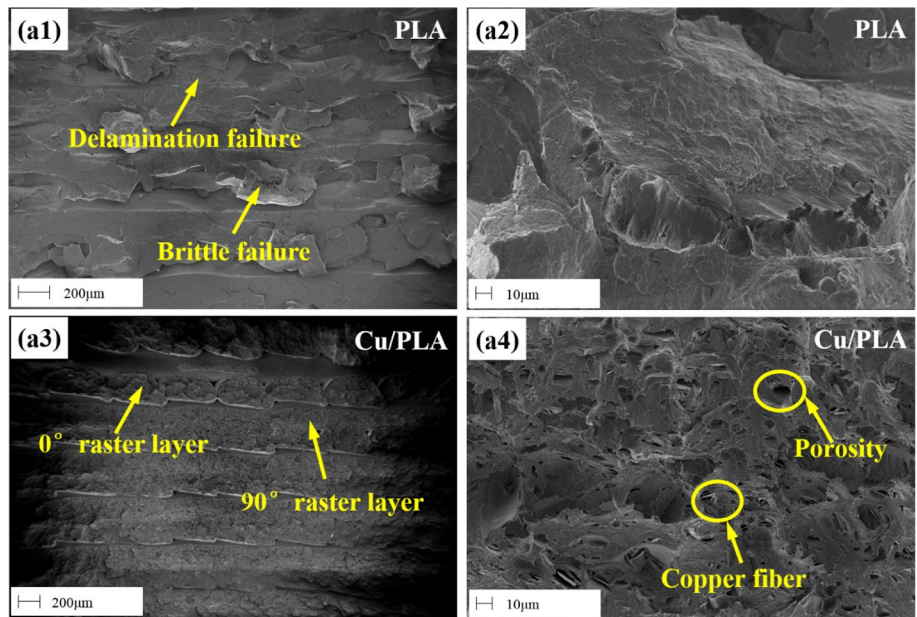
Fig. 14 Schematic showing the fracture modes of the additive manufactured PLA and Cu/PLA undergone tensile test at different raster angles. **a** 0°, **b** 90°, **c** 45°, **d** ±45° and **e** 0°/90°

number of fuses side by side. When the external load pulls all the fuses of each layer, the specimen will fail. Therefore, the tensile stress must be greater than the strength of all fuses to pull off the specimen.

For 90° raster angle specimen, the tensile loading is applied vertical to the raster layers. The failure mechanism depends on the adhesion between adjacent raster layers. Compared with the 0° raster angle specimen, the bond between raster layers of 90° specimen exhibits a weaker capacity. According to the analysis of fracture surface morphology in Fig. 10, under the tensile testing, the stress is concentrated on the bonding area of the inter-layer, and the specimen fails under delamination of layers from bonded region. Since many physical gaps exist in adjacent layers, the adhesion between the raster layers is poor. Figure 6 shows that less tensile load is required to break the specimen, which indicates that tensile strength is relatively lower compared to 0° raster layer specimen.

When the applied loaded tensile load is 45° from the direction of the raster layers, the load bearing mechanism of the raster layers is completely different from 0° and 90° orientation. The tensile load (F) is broken down into two direction forces, namely parallel (F_t) and perpendicular (F_a) to the direction of raster layer (Fig. 14c). When the perpendicular load (F_a) is applied to the specimen, the failure mechanism of the specimen is consistent with the 90° raster angle (inter-layer fracture), while under applied parallel load, it is consistent with the 0° raster angle (intra-layer fracture). Due to the poor adhesion between the raster layers, the separation of the inter-layer bond region first occurred under perpendicular load (F_a).

Idealizations of the ± 45° raster orientations for FDM specimen is shown in Fig. 14d. The tensile load aligned parallel to the length of the specimen is applied. The load (F) can also be decomposed into two mutually perpendicular component forces, F_t and F_a, respectively. For the +45° raster layers, they must withstand the normal stress from F_a and the shear stress from F_t. Similarly, the normal stress and shear stress act simultaneously on the −45° raster layers. That is to say, for these two different raster layers (+45° and −45°), inter-layer and intra-layer fracture occur simultaneously.

Combined with the tensile strength results and fracture morphologies of specimens with 0°/90° raster angle, the 0° raster layers requires a large stress to allow the crack to spread to the entire fracture surface, resulting in a final failure (Fig. 13). Since the 90° raster layer is vertical to the loading direction, it represents a weak load capacity. Thus delimitation of the 90° raster layer exposing the 0° raster layer shows that the 90° raster layers is first separated from the adjacent raster layers under tensile load (fracture initiation from these regions), while 0° raster layers are a tear and rupture of individual raster layers (final failure starts from these regions).

In addition, the tensile strength of Cu/PLA is lower than that of pure PLA. The stress transfer determines the mechanical properties of the composites. Due to the different elasticity of the copper fiber and the PLA matrix, the interfacial adhesion is not strong enough. Therefore, when the stress is higher than the bond strength at the interface, porosities form due to the fiber pull-outs.

4 Conclusions

In this study, polymer-metal composite specimens are prepared by 3D printing based on FDM. The specimens are printed at varied raster angles (at 0°, 90°, 45°, 0°/90° and ± 45°). The effect of raster angles on tensile properties and dynamic mechanical properties of specimens are studied. Fracture surface of specimens after tensile testing is observed by SEM, and the fracture mode is also analyzed.

Dynamic mechanical thermal analysis demonstrates that thermal stability of PLA can be improved by the addition of reinforced copper fibers. The maximum storage modulus recorded for PLA specimen with 0° raster angle is 3.13 GPa, whereas for Cu/PLA specimen is 3.29 GPa.

The maximum tensile strength recorded for PLA and Cu/PLA specimens with 0° raster angle are 68.1 MPa and 44.2 MPa, respectively, while the 90° raster angle with the lowest value (PLA: 52.9 MPa; Cu/PLA: 36.1 MPa). Fracture morphologies indicate that the failure of a specimen at 0° raster angle is intra-layer fracture, while inter-layer fracture occur in the specimen at 90° raster angle. Because of the lower tensile strength and higher elasticity of Cu fiber compared with PLA, the tensile strength of Cu/PLA composite specimen decreases with the addition of copper fiber, however, the elongation-at-break increases.

It can be seen from the research that by controlling the parameters of FDM processing, it is of great potential to process some functional components such as thermal conductivity and magnetic properties with polymer-metal composites as raw materials. In addition, in order to make polymer-metal composites more widely used in the industry, there is still much room for improvement in the performance of printed parts, for example, changing the proportion of metal fibers in composites, optimizing printing parameters or developing more polymer-metal composites.

Compliance with ethical standards

Conflict of interest The authors declare that they have no conflict of interest.

References

1. Sames WJ, List FA, Pannala S, Dehoff RR, Babu SS (2016) The metallurgy and processing science of metal additive manufacturing. Int Mater Rev 61(5):315–360
2. Kalsoom U, Nesterenko PN, Paull B (2016) Recent developments in 3D printable composite materials. RSC Adv 6(65):60355–60371
3. Farina I, Fabbrocino F, Colangelo F, Feo L, Fraternali F (2016) Surface roughness effects on the reinforcement of cement mortars through 3D printed metallic fibers. Compos Pt B-Eng 99:305–311
4. Farina I, Fabbrocino F, Carpentieri G, Modano M, Amendola A, Goodall R, Feo L, Fraternali F (2016) On the reinforcement of cement mortars through 3D printed polymeric and metallic fibers. Compos Pt B-Eng 90:76–85
5. Hager I, Golonka A, Putanowicz R (2016) 3D printing of buildings and building components as the future of sustainable construction? Procedia Eng 151:292–299
6. Goh GD, Agarwala S, Goh GL, Dikshit V, Sing SL, Yeong WY (2017) Additive manufacturing in unmanned aerial vehicles (UAVs): challenges and potential. Aerosp Sci Technol 63:140–151
7. Jamroz W, Szafraniec J, Kurek M, Jachowicz R (2018) 3D printing in pharmaceutical and medical applications—recent achievements and challenges. Pharm Res 35(9):22
8. Duregger K, Trik S, Leonhardt S, Eblenkamp M (2018) Additive-manufactured microporous polymer membranes for biomedical in vitro applications. J Biomater Appl 33(1):116–126
9. Moiduddin K (2018) Implementation of computer-assisted design, analysis, and additive manufactured customized mandibular implants. J Med Biol Eng 38(5):744–756
10. Wen P, Jauer L, Voshage M, Chen YZ, Poprawe R, Schleifenbaum JH (2018) Densification behavior of pure Zn metal parts produced by selective laser melting for manufacturing biodegradable implants. J Mater Process Technol 258:128–137
11. Campbell I, Bourell D, Gibson I (2012) Additive manufacturing: rapid prototyping comes of age. Rapid Prototyp J 18(4):255–258
12. Brenken B, Barocio E, Favaloro A, Kunc V, Pipes RB (2018) Fused filament fabrication of fiber-reinforced polymers: a review. Addit Manuf 21:1–16
13. Gurrala PK, Regalla SP (2014) Part strength evolution with bonding between filaments in fused deposition modelling: this paper studies how coalescence of filaments contributes to the strength of final FDM part. Virtual Phys Prototype 9(3):141–149
14. Sun Q, Rizvi GM, Bellehumeur CT, Gu P (2008) Effect of processing conditions on the bonding quality of FDM polymer filaments. Rapid Prototype J 14(2):72–80
15. Sood AK, Ohdar RK, Mahapatra SS (2010) Parametric appraisal of mechanical property of fused deposition modelling processed parts. Mater Des 31(1):287–295
16. Jones R, Haufe P, Sells E, Iravani P, Olliver V, Palmer C, Bowyer A (2011) RepRap—the replicating rapid prototyper. Robotica 29:177–191
17. Zhong S, Pearce JM (2018) Tightening the loop on the circular economy: coupled distributed recycling and manufacturing with recyclebot and RepRap 3-D printing. Resour Conserv Recycl 128:48–58
18. Anzalone GC, Wijnen B, Pearce JM (2015) Multi-material additive and subtractive prosumer digital fabrication with a free and open-source convertible delta RepRap 3-D printer. Rapid Prototype J 21(5):506–519
19. de Ciurana J, Sereno L, Valles E (2013) Selecting process parameters in RepRap additive manufacturing system for PLA scaffolds manufacture. In: Mitsuishi M, Bartolo P (eds) First Cirp conference on biomanufacturing, pp 152–157
20. Gomez-Gras G, Jerez-Mesa R, Travieso-Rodriguez JA, Lluma-Fuentes J (2018) Fatigue performance of fused filament fabrication PLA specimens. Mater Des 140:278–285
21. Srivatsan T, Sudarshan T (2015) Additive manufacturing: innovations advances and applications. CRC Press, Boca Raton
22. Galantucci LM, Lavecchia F, Percoco G (2009) Experimental study aiming to enhance the surface finish of fused deposition modeled parts. CIRP Ann-Manuf Technol 58(1):189–192
23. Kalita SJ, Bose S, Hosick HL, Bandyopadhyay A (2003) Development of controlled porosity polymer-ceramic composite scaffolds via fused deposition modeling. Mater Sci Eng C-Biomimetic Supramol Syst 23(5):611–620
24. Ahn SH, Montero M, Odell D, Roundy S, Wright PK (2002) Anisotropic material properties of fused deposition modeling ABS. Rapid Prototyp J 8(4):248–257
25. Huang B, Singamneni S (2015) Raster angle mechanics in fused deposition modelling. J Compos Mater 49(3):363–383
26. Nancharaiah T, Raju DR, Raju VR (2010) An experimental investigation on surface quality and dimensional accuracy of FDM components. Int J Emerg Technol 1(2):106–111
27. Durgun I, Ertan R (2014) Experimental investigation of FDM process for improvement of mechanical properties and production cost. Rapid Prototype J 20(3):228–235
28. Onwubolu GC, Rayegani F (2014) Characterization and optimization of mechanical properties of ABS parts manufactured by the fused deposition modelling process. Int J Manuf Eng
29. Quill TJ, Smith MK, Zhou T, Baioumy MGS, Berenguer JP, Cola BA, Kalaitzidou K, Bougher TL (2018) Thermal and mechanical properties of 3D printed boron nitride—ABS composites. Appl Compos Mater 25(5):1205–1217
30. Melenka GW, Cheung BKO, Schofield JS, Dawson MR, Carey JP (2016) Evaluation and prediction of the tensile properties of continuous fiber-reinforced 3D printed structures. Compos Struct 153:866–875
31. Li N, Li Y, Liu S (2016) Rapid prototyping of continuous carbon fiber reinforced polylactic acid composites by 3D printing. J Mater Process Technol 238:218–225
32. Shofner ML, Lozano K, Rodriguez-Macias FJ, Barrera EV (2003) Nanofiber-reinforced polymers prepared by fused deposition modeling. J Appl Polym Sci 89(11):3081–3090
33. Zhong WH, Li F, Zhang ZG, Song LL, Li ZM (2001) Short fiber reinforced composites for fused deposition modeling. Mater Sci Eng A-Struct Mater Prop Microstruct Process 301(2):125–130
34. Ponnamma D, Cabibihan JJ, Rajan M, Pethaiah SS, Deshmukh K, Gogoi JP, Pasha SKK, Ahamed MB, Krishnegowda J, Chandrashekar BN, Polu AR, Cheng C (2019) Synthesis, optimization and applications of ZnO/polymer nanocomposites. Mater Sci Eng C-Mater Biol Appl 98:1210–1240
35. Sankaran S, Deshmukh K, Ahamed MB, Pasha SKK (2018) Recent advances in electromagnetic interference shielding properties of metal and carbon filler reinforced flexible polymer composites: a review. Compos Pt A-Appl S 114:49–71

36. Yu T, Ren J, Li S, Yuan H, Li Y (2010) Effect of fiber surface-treatments on the properties of poly(lactic acid)/ramie composites. Compos Pt A-Appl S 41(4):499–505

37. Liao G, Li Z, Cheng Y, Xu D, Zhu D, Jiang S, Guo J, Chen X, Xu G, Zhu Y (2018) Properties of oriented carbon fiber/polyamide 12 composite parts fabricated by fused deposition modeling. Mater Des 139:283–292

38. McLouth TD, Severino JV, Adams PM, Patel DN, Zaldivar RJ (2017) The impact of print orientation and raster pattern on fracture toughness in additively manufactured ABS. Addit Manuf 18:103–109

39. Papon EA, Haque A (2018) Tensile properties, void contents, dispersion and fracture behaviour of 3D printed carbon nanofiber reinforced composites. J Reinf Plast Compos 37(6):381–395

40. Garg A, Bhattacharya A (2017) An insight to the failure of FDM parts under tensile loading: finite element analysis and experimental study. Int J Mech Sci 120:225–236